# Chapter 5

# Basic simulations of transducer sound fields

In this chapter, the numerical method developed in the last chapter is applied to basic simulation problems as well as to the calculation of A-scans. In the first section, simulations of basic transducer sound fields in isotropic and anisotropic materials are shown. The implemented defect types are discussed and simulations of the scattering of the sound field on these are shown. As will be illustrated, for anisotropic materials the interpretation of such simulations may be extremely challenging.

The second section continues the discussion from the last chapter on A-scan modelling. An alternative A-scan model to the simple one presented in the previous chapter is presented and the two models are compared for a few included defects. Furthermore, the SUNDT program discussed in section 2.6 is compared with these two models.

## 5.1 Basic simulations of transducer sound fields

In this section, examples of sound fields from different types of transducers are shown. In all the examples considered, the materials considered are homogeneous. In the first plots, the material is isotropic and the characteristics of the sound field are well-known. In the last plots, the material is anisotropic. These may serve to illustrate how fundamentally different wave propagation in anisotropic materials is as compared to isotropic materials.

Fig. 5.1 shows the sound field for a $0°$ transducer with a pulse signal $f(t;2)$ (the Panametrics transducer) and $f_0 = 2\,\text{MHz}$ in isotropic austenite at time $t = 5\,\mu\text{s}$, where the different wave fronts are clearly illustrated. The longitudinal (L), transverse (T), head (H) and Rayleigh (R) wave are shown. In this case the transverse wave is rather weak relative to the longitudinal wave. The head wave was met earlier for an anisotropic material in Fig. 3.13, but here a basic description of the wave type will be given in the isotropic case. The wave originates at the surface together with the longitudinal wave and ends at the point on the transverse spherical wave where it is perpendicular to radius vector. From the figure, clearly the angle $\theta$ of the head wave with respect to vertical is $\sin\theta = v_t/v_l$. Thus, the angle only depends on the two wave velocities in the material. As illustrated by arrows, a point $(x_1, x_3)$ on the wave front first travels a distance $x_1 - x_3((v_l/v_t)^2 - 1)^{-1/2}$ along the surface as a longitudinal wave (with velocity $v_l$) and then an additional distance $x_3(1 - (v_t/v_l)^2)^{-1/2}$ as a transverse wave (with velocity $v_t$). In the following, similar plots

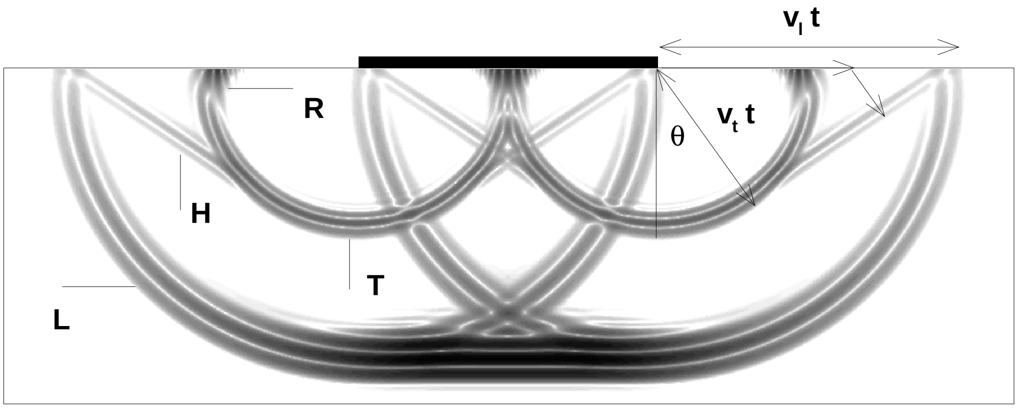


Figure 5.1: Contour plot of $|\boldsymbol{v}|$ at time $t = 5\,\mu$s for a 0° transducer of width 26.6 mm and with a pulse signal $f(t;2)$ and $f_0 = 2$MHz. The material is isotropic austenite, Table 2.1, with dimensions 90 mm × 30 mm. Logarithmic scale with range 0 dB (black) to -50 dB (white) with 25 levels. $(\Delta x, \Delta t) = (10^{-4}\,\mathrm{m}, 10^{-8}\,\mathrm{s})$.

for angled transducers will be presented with head waves being present in these as well. However, as will be seen the angle of propagation of these waves is not influenced by the transducer which is to be expected from the above considerations.

Fig. 5.2 shows the same situation as in Fig. 5.1 but for a pulse signal $f(t;5)$. As expected, the different wave types are far more spread out compared to the previous figure.

Fig. 5.3 shows a longitudinal 45° transducer with pulse shape $f(t;2)$ and $f_0 = 2\,$MHz at the two points in time, $t = 4.5\,\mu$s (left) and $t = 9.0\,\mu$s (right). Note the similarity of the head waves in the plot with those in Fig. 5.1. Fig. 5.4 shows the same situation but with a pulse shape $f(t;5)$ (the RTD transducer).

The final situation for the isotropic material is that of a focused transducer as shown in Fig. 5.5. This is just one example of how a phased array may be operated. The pulse signal is again $f(t;2)$ with $f_0 = 2\,$MHz. The point of focus is at a depth 15 mm below the transducer which is where the two lines cross. The two lines indicate the area, where the sound field is focusing in the sense that at each point on the wave front, the wave vector is directed towards the point of focus. The sound field is shown at three instances in time, $t = 2.0$, 4.0 and 6.0 $\mu$s. In the upper and lower plot the wave fronts show up in the characteristic parabolic shape.

In the remaining part of this section, wave propagation in anisotropic materials is modelled. The material considered is the transversely isotropic material X 6 CrNi 18 12 (Table 2.3 on p. 23) for different orientations of the symmetry axis. Fig. 5.6 shows the situation in case of the symmetry axis being parallel to the $x_3$-axis. The transducer is a 0° transducer with a pulse signal $f(t;2)$ and $f_0 = 2\,$MHz. Time is $t = 4.5\,\mu$s. Thus, the wave normal under the transducer is parallel to the symmetry axis and no beam skewing is present for the qL wave and the qSV wave according to Fig. 3.4. The qL wave is somewhat similar to the pure L wave in Fig. 5.1 and the accompanying quasi head waves are also clearly present. The characteristic shape of the qSV wave is recognized from Fig. 3.3. As

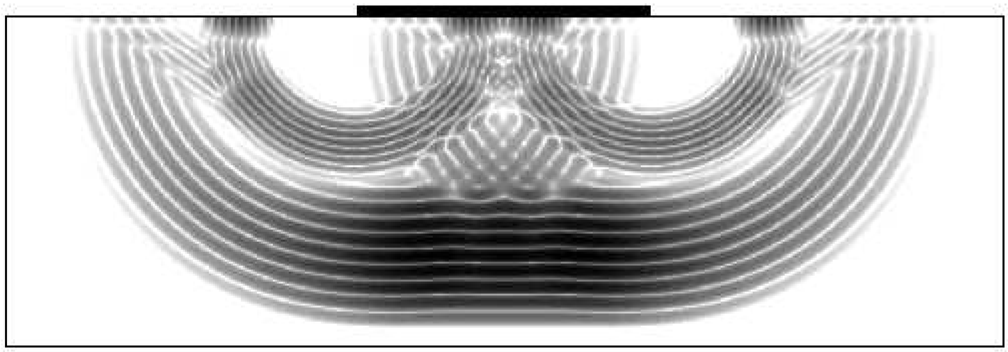

Figure 5.2: Contour plot of $|\boldsymbol{v}|$ at time $t = 5\,\mu$s for a 0° transducer of width 26.6 mm and with a pulse signal $f(t;5)$ and $f_0 = 2$MHz. The material is isotropic austenite, Table 2.1, with dimensions 90 mm × 30 mm. Logarithmic scale with range 0 dB (black) to -50 dB (white) with 25 levels. $(\Delta x, \Delta t) = (10^{-4}\,\mathrm{m}, 10^{-8}\,\mathrm{s})$.

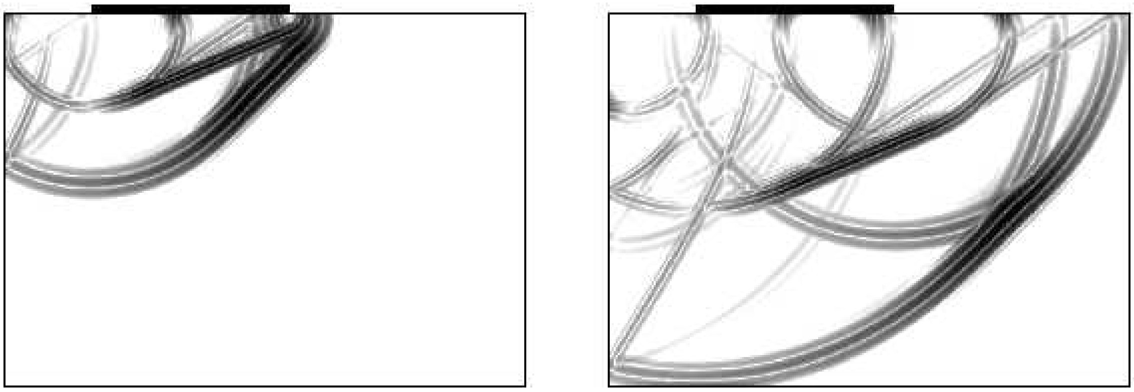

Figure 5.3: Contour plot of $|\boldsymbol{v}|$ for a longitudinal 45° transducer of width 26.6 mm with pulse signal $f(t;2)$ and $f_0 = 2\,$MHz. Material is isotropic austenite. Dimensions are 70 mm × 50 mm. Left plot: $t = 4.5\,\mu$s. Right plot: $t = 9.0\,\mu$s. Logarithmic scale with range 0 dB (black) to -50 dB (white) with 25 levels. $(\Delta x, \Delta t) = (10^{-4}\,\mathrm{m}, 10^{-8}\,\mathrm{s})$.

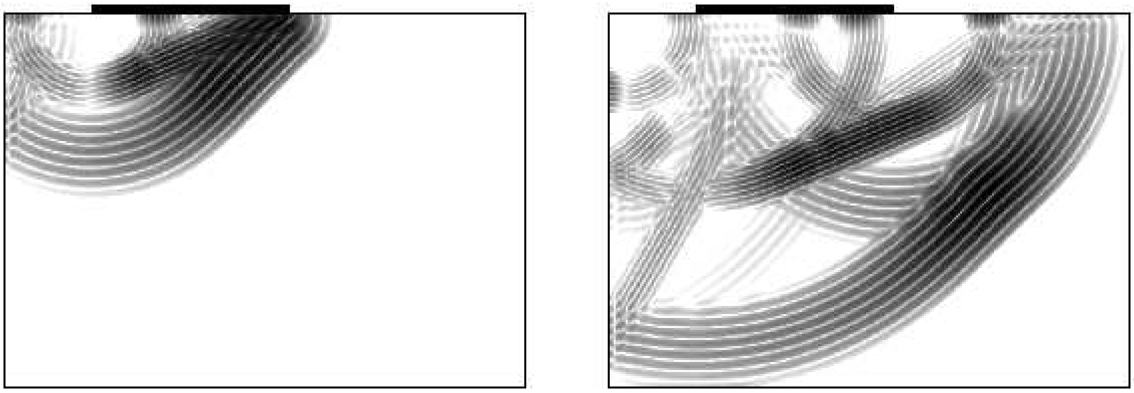

Figure 5.4: Contour plot of $|\boldsymbol{v}|$ for a longitudinal 45° transducer of width 26.6 mm with pulse signal $f(t;5)$ and $f_0 = 2\,\text{MHz}$. Material is isotropic austenite. Dimensions are 70 mm $\times$ 50 mm. Left plot: $t = 4.5\,\mu\text{s}$. Right plot: $t = 9.0\,\mu\text{s}$. Logarithmic scale with range 0 dB (black) to -50 dB (white) with 25 levels. $(\Delta x, \Delta t) = (10^{-4}\,\text{m}, 10^{-8}\,\text{s})$.

opposed to the case of the qL wave, there is no plane wave front associated with the qSV wave. Compare also with Fig. 3.13 showing the basic sound field from a line source.

Fig. 5.7 shows the same situation as in the previous figure, but with a symmetry axis rotated an (Euler) angle $\theta = -49.1°$ around the $x_2$-axis. As described previously, the rotation of the elastic matrix has been calculated using (2.22) with $\boldsymbol{M}(0, \theta, 0)$. According to Fig. 3.4 there is no beam skewing of the qL wave. This is in agreement with the plot, showing a qL wave propagating downwards below the transducer. Note, how the horizontal plane wave front of the qL wave is of much smaller extent that in the previous figure. Beam skewing is taking place for the qSV wave with an angle of approximately $\Delta = 27°$. The effect of this is best appreciated by comparing with the previous figure where no beam skewing is present. Also for this plot there is no plane wave front present for the qSV wave. Note the apparent lack of symmetry in the plot due to the rotation of the symmetry axis.

Fig. 5.8 illustrates the case of a 45° transducer with $f(t;2)$ and $f_0 = 2\,\text{MHz}$ applied to the material in it's unrotated state, i. e. with the symmetry axis pointing downwards. The plots show the sound field at time steps $t = 4.5, 9.0\,\mu\text{s}$. The plane wave fronts of the qSV and the qL waves are clearly observed. The quasi head waves are also seen. Using Snell's law in a computational approach or the simpler geometrical approach as in Fig. 3.5 (right) involving the previously described plexiglas and X 6 CrNi 18 12 with an angle of incidence equal to 20° the refracted angles of the qL wave and the qSV wave are found to be 51.5° and 22.3° respectively which may be verified in the figure. From Fig. 3.4, only a small angle of beam skewing equal to $\Delta = -1.7°$ is present for the qL wave. For the qSV wave the beam skewing is quite severe, with an angle of $\Delta = -44.6°$. The effect is clearly seen in the right figure. The qSV wave is propagating through the left boundary, while the qL wave behaves almost as an ordinary L wave in an isotropic material. Compare with the refracted waves in the equivalent situation in Fig. 5.3.

In Fig. 5.9 the symmetry axis has been rotated the Euler angle $\theta = -20°$. The rotation

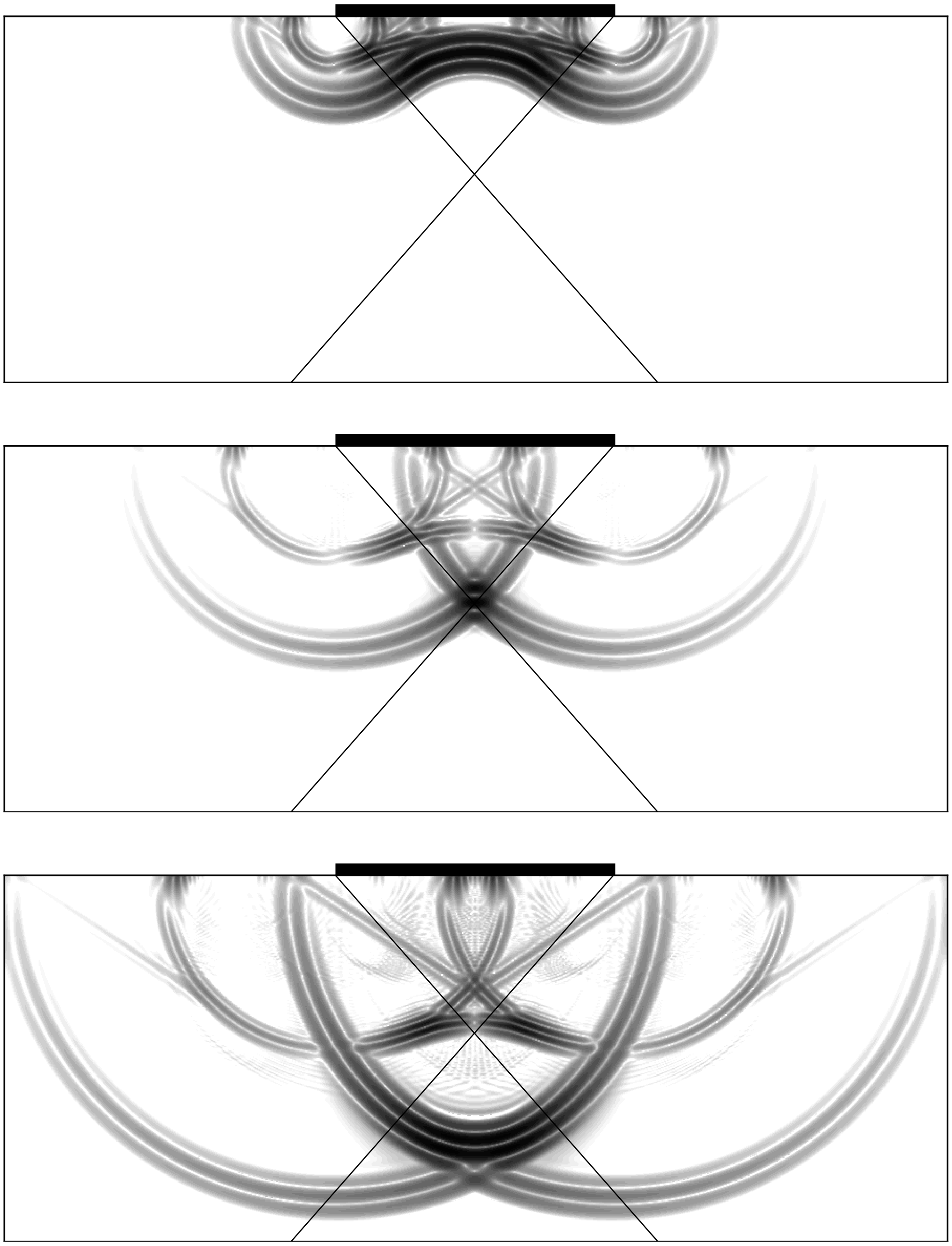

Figure 5.5: Contour plot of focused transducer of width 26.6 mm with pulse signal $f(t;2)$ and $f_0 = 2\,\mathrm{MHz}$. Point of focus is 15 mm below the transducer where lines cross. Material is isotropic austenite. Times are $t = 2.0$, 4.0 and 6.0 $\mu$s. Dimensions are 90 mm $\times$ 35 mm. Logarithmic scale with range 0 dB (black) to -50 dB (white) with 25 levels. $(\Delta x, \Delta t) = (10^{-4}\,\mathrm{m}, 10^{-8}\,\mathrm{s})$.

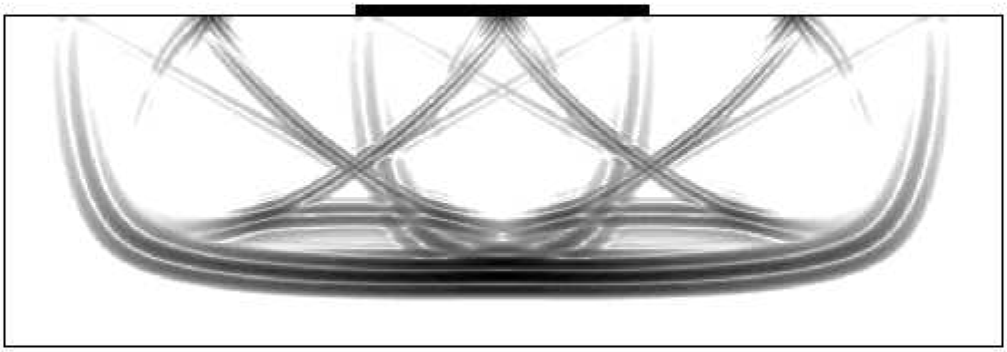

Figure 5.6: Contour plot of $|\boldsymbol{v}|$ for a 0° transducer of width 26.6 mm with a pulse signal $f(t;2)$ and $f_0 = 2\,\text{MHz}$. Time is $t = 4.5\,\mu\text{s}$. The material is transversely isotropic X 6 CrNi 18 12 with a vertical symmetry axis. Dimensions are 90 mm × 30 mm and time is $t = 5\,\mu\text{s}$. Logarithmic scale with range 0 dB (black) to -50 dB (white) with 25 levels. $(\Delta x, \Delta t) = (10^{-4}\,\text{m}, 10^{-8}\,\text{s})$.

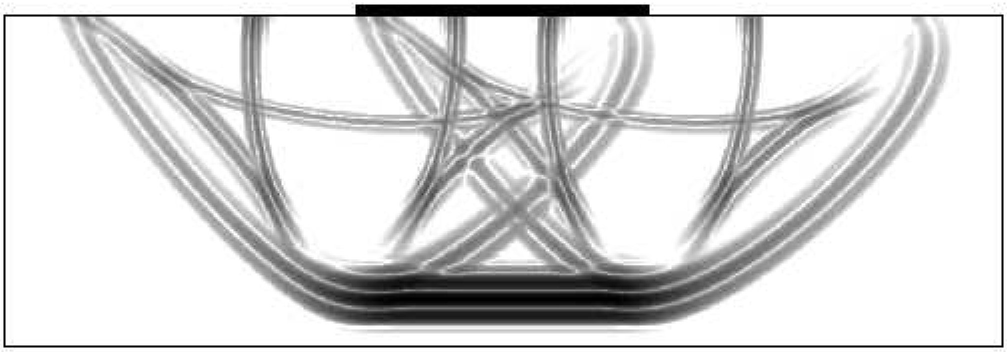

Figure 5.7: Contour plot of $|\boldsymbol{v}|$ for a 0° transducer of width 26.6 mm with a pulse signal $f(t;2)$ with $f_0 = 2\,\text{MHz}$. The material is the transversely isotropic X 6 CrNi 18 12 with the symmetry axis rotated the Euler angle $\theta = -49.1°$. Dimensions are 90 mm × 30 mm and time is $t = 4.5\,\mu\text{s}$. Logarithmic scale with range 0 dB (black) to -50 dB (white) with 25 levels. $(\Delta x, \Delta t) = (10^{-4}\,\text{m}, 10^{-8}\,\text{s})$.

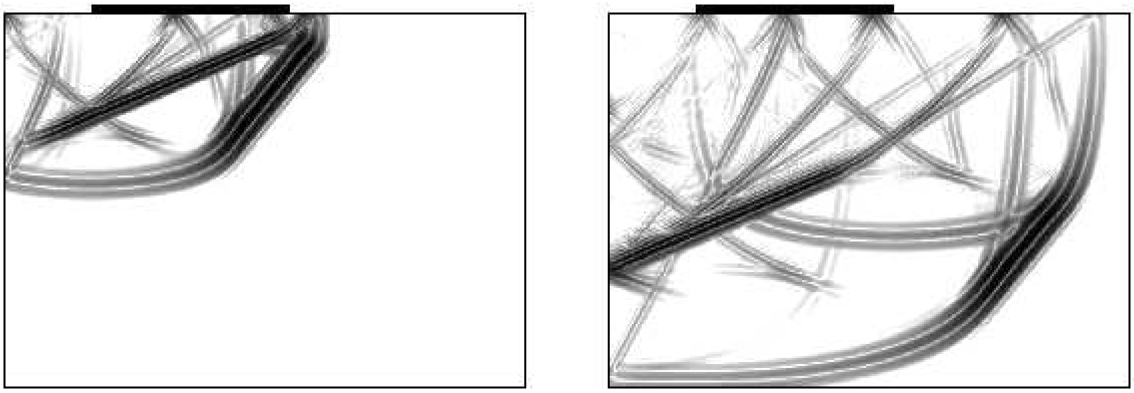

Figure 5.8: Contour plot of $|\boldsymbol{v}|$ for a longitudinal 45° transducer of width 26.6 mm with pulse signal $f(t;5)$. Material is the transversely isotropic X 6 CrNi 18 12 with vertical symmetry axis. Left: $t = 4.5\,\mu$s. Right: $t = 9.0\,\mu$s. Dimensions are 70 mm × 50 mm. Logarithmic scale with range 0 dB (black) to -50 dB (white) with 25 levels. $(\Delta x, \Delta t) = (10^{-4}\,\mathrm{m}, 10^{-8}\,\mathrm{s})$.

has been performed as described above. The resulting numerical elastic matrix is shown in (5.1). Apart from the change in values of existing elastic constants, elastic constants that originally were zero now have a finite value. However, the form of the elastic matrix of course still belongs to the monoclinic class with the matrix (2.33).

$$\boldsymbol{c}' = \begin{pmatrix} 2.91 & 1.04 & 1.11 & 0.0 & -0.327 & 0.0 \\ & 2.63 & 1.40 & 0.0 & -1.50 & 0.0 \\ & & 2.55 & 0.0 & 0.478 & 0.0 \\ & & & 1.24 & 0.0 & -1.50 \\ & & & & 0.952 & 0.0 \\ & & & & & 0.878 \end{pmatrix} \times 10^{11} Pa \tag{5.1}$$

For a 0° transducer as above (with a pulse signal $f(t;2)$ and $f_0 = 2\,\mathrm{MHz}$) this rotation results in a large beam skewing according to Fig. 3.4 with angle $\Delta = -44°$ for the qL wave and an angle $\Delta = 20°$ for the qSV wave. To illustrate the effect of beam skewing further, four plots are shown at different time steps $t = 2.5, 5.0, 7.5, 10\,\mu$s. In the first plot, the wave vector $\boldsymbol{k}$ together with the energy vectors $\boldsymbol{v}_{g,qL}$ and $\boldsymbol{v}_{g,qSV}$ of the corresponding qL and qSV respectively are shown. In these plots, a plane wave is observed for the qSV wave. It is seen how the qL wave travels in one direction while the qSV travels in the other direction relative to the wave vector. The qL wave is then reflected at the backwall and is finally detected by the transducer.

To the inexperienced observer it may seem as if Snell's law governing the angles of incidence and reflection is violated. However, Snell's law governs the wave vector. Before reaching the backwall, the wave vector is pointing vertically downwards (zero angle of incidence) and after reflection the wave vector is pointing vertically upwards (zero angle of reflection). It is the anisotropy and the role which the energy vector plays in these materials that result in these highly unusual phenomena.

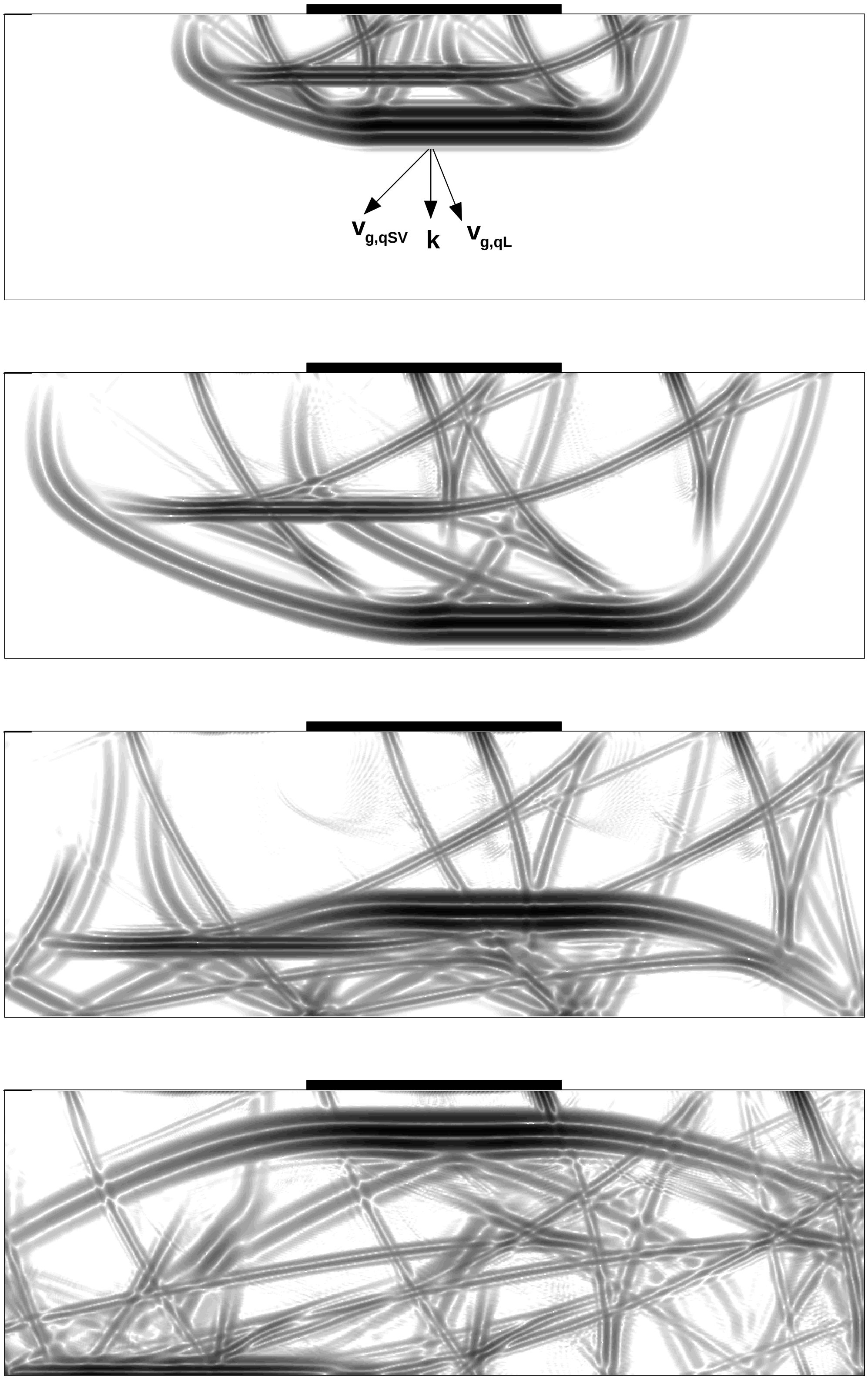


Figure 5.9: Contour plot of $|\boldsymbol{v}|$ for a $0°$ transducer of width 26.6 mm with a pulse signal $f(t;2)$ with $f_0 = 2\,\mathrm{MHz}$. The material is the transversely isotropic X 6 CrNi 18 12 with the symmetry axis rotated the Euler angle $\theta = -49.1°$. Dimensions are 90 mm $\times$ 30 mm and times are $t = 2.5, 5.0, 7.5, 10\,\mu\mathrm{s}$. Logarithmic scale with range 0 dB (black) to -50 dB (white) with 25 levels. $(\Delta x, \Delta t) = (10^{-4}\,\mathrm{m}, 10^{-8}\,\mathrm{s})$.

The plots also illustrate another important aspect of ultrasonic inspection. If, in an ultrasonic testing operation, the operator assumes that the material is isotropic, he may be misled by the received signal, knowing that it is a $0°$ transducer, to place the (small) reflector right below the transducer instead of at an angle to the transducer. The height of the reflector in the material is furthermore likely to be misjudged based on the recorded time of travel.

In this section, plots of different basic sound fields have been shown for an isotropic and an anisotropic material. Especially in the case of the anisotropic material, it has been illustrated how parts of the (non-intuitive) behaviour qualitatively may be explained using results from time harmonic plane wave theory. This may be commented on from two points of view. On one hand, it directly shows that this simple theory may explain in a qualitative way certain important aspects of wave propagation in anisotropic materials. On the other hand, very often when working with numerical solutions it may be difficult to interpret the solution as the numerical approach doesn't reveal information concerning the way the solution is obtained. It may therefore be of high importance, that basic theoretical explanations are available. We shall see another example of this in the next section.

## 5.2 Interior defects with stress free boundaries

In this section, the different types of defect geometries which have been implemented in the modelling program will be described and a number of simulations will be shown in order to illustrate the different types of waves that are generated as a result of the presence of the defect.

It has previously been mentioned, that since the (anisotropic) inhomogeneous formulation of the elastodynamic equations is considered in the numerical solution, impurities or more generally inhomogeneities with different material properties than those of the parent material are automatically handled by the numerical solution. However, an example of an important type of defect is the crack, which is modelled as being a small isolated volume of vacuum. This requires explicit boundary conditions in the form of a stress free boundary in the same way as the material geometry is modelled in this thesis.

Two essentially different geometries with stress free boundaries have been implemented. The first is a circular geometry which may have an arbitrary radius and an arbitrary position of the center. The second is a rectangular shape, which may have an arbitrary height and width and with the axis arbitrarily oriented. It should be noted, that these geometries have been implemented on a grid consisting of quadratic elements (2D). This means that in the case of the circular geometry and for a tilted rectangular geometry, a stair-case approximation has been used to describe the true geometry. A theoretical analysis of the errors introduced through this approximation has not been carried out. The problem is addressed in [19] concerning the solution to Maxwell's equations using the finite-difference approach. It is concluded, that by making the grid sufficiently fine, artificial phenomena may be made arbitrarily small. The problem is also considered in [47] where the numerical solution is compared to the analytic solution in the case of a circular geometry (airfilled cylinder) placed in an isotropic material for different values of the radius. As an example, for a radius $r = 12\Delta x = 3\,\mathrm{mm}$ the relative error in amplitude of the echo signal is 4.8% and vanishes for increasing radius. These issues are of importance when comparing this method with other methods, such as an analytic approach, where a circle may be modelled as a true circle and likewise for a tilted rectangular crack. However, in a real ultrasonic inspection, the defects are neither perfect circles nor tilted rectangular cracks. The staircase approximation applied here as an approximation is in principle thus neither more nor less correct than more smooth geometry representations.

A solution to the problem of an incident time harmonic longitudinal plane wave on a half plane with a stress free boundary (a semi-infinite crack) was first formulated by Maue in [50] and has since then been restated in various ways, e.g. [2]. Before considering a complete modelling situation, it is instructive to consider the wave fronts of the generated waves at the crack tip for an incoming time harmonic longitudinal plane wave as obtained in f. ex. [2]. These wave fronts are shown in Fig. 5.10. The incident wave gives raise to

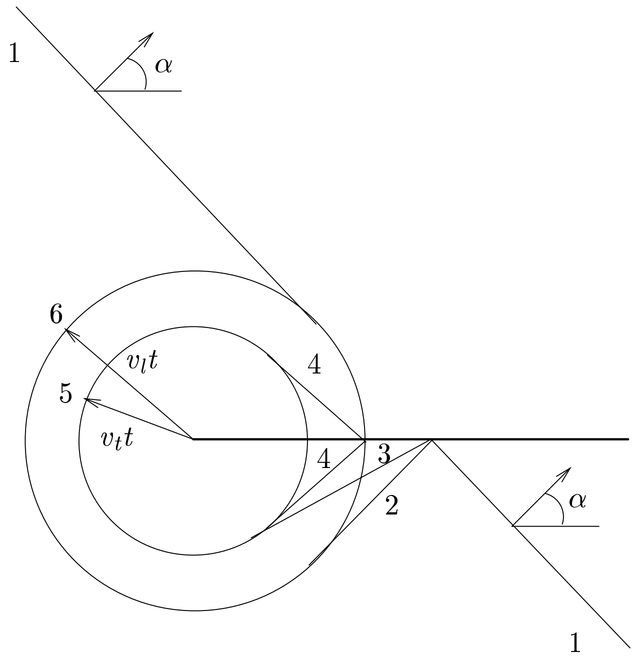


Figure 5.10: Wave fronts of the generated waves at a crack tip from an incomning longitudinal wave at an angle $\alpha$. The different waves are: 1 = incoming longitudinal wave at an angle $\alpha$, 2 = reflected longitudinal wave, 3 = reflected transverse wave, 4 = head wave, 5 = diffracted transverse wave, 6 = diffracted longitudinal wave.

the well-known reflected and refracted plane waves away from the crack tip. Furthermore, two diffracted waves of longitudinal and transverse nature with center at the crack tip are generated with radius $v_l t$ and $v_t t$ respectively at time $t$. Associated with the diffracted longitudinal wave is the head wave. In addition to the diffracted transverse wave, a Rayleigh wave (not shown) is generated at the surface. Thus, the effect of the isolated crack tip is much the same as that for the line source at the free surface considered earlier.

In the case of an incoming SH wave only a diffracted wave of SH nature is generated apart from a reflected SH wave. As previously mentioned, this is because the wave does not couple to the L wave and SV wave. Thus the generated picture is much simpler.

In the rest of this section, examples of scattered fields are shown for different rectangular crack orientations as well as of circular cavities. First, the well-known isotropic case is considered followed by the more complex anisotropic case, where the interpretation of the generated field may become rather challenging.

Fig. 5.11 shows the scattered sound field for several different orientations of a rectangular crack of height 20 mm in isotropic austenite (compare with the undisturbed field in Fig. 5.1 in the case of no crack present). The incident field is from a 0° transducer of width 26.6 mm with pulse signal $f(t;2)$ and $f_0 = 2\,\mathrm{MHz}$. The times are $t = 6.8\,\mu\mathrm{s}$ (upper and middle plot) and $t = 5.8\,\mu\mathrm{s}$ (lower). In each case, the interesting part of the scattered field is identified. In the upper most simple plot with a crack width equal to 0.1 mm, the diffracted longitudinal (DL) and transverse (DT) waves, the head (H) waves and the Rayleigh (R) waves are clearly seen. In the middle plot with a crack width equal to 0.2 mm, the crack is tilted 45°. Apart from the above mentioned scattered waves, the reflected longitudinal (RL) and transverse (RT) waves are also seen. Also note the shadow zone on the back side. Clearly, the reflected transverse wave has the larger amplitude compared to the reflected longitudinal wave. This is in agreement with the theory of wave scattering of plane waves at a boundary. In the isotropic case, this problem may be solved analytically with particular simple results at a stress free boundary for the relative amplitude coefficients, see [8]. For the considered isotropic austenite with an 45° incident longitudinal wave, the relative amplitude coefficient for the reflected longitudinal wave is -0.4048 and for the reflected transverse wave 1.085, corresponding to a difference of 8.5639 dB in amplitudes. It is difficult to isolate these two waves in the middle plot, but probings at different positions show that the amplitudes in the numerical solution are in reasonable agreement with these values. In the lower plot with a crack width equal to 0.1 mm, the case of a horizontal crack is considered. Fields propagate along the back side and front side of the crack.

Fig. 5.12 shows the complex scattered fields for a probe field and rectangular crack orientations as in Fig. 5.11 but in the case of the transversely isotropic material X 6 CrNi 18 12 rotated the Euler angle $\theta = -20°$ around the $x_2$-axis. This case was also considered in Fig. 5.9 exhibiting a large beam skewing effect. The times are again $t = 6.8\,\mu\mathrm{s}$ (upper and middle plot) and $t = 5.8\,\mu\mathrm{s}$ (lower). An attempt has been made to identify the different interesting parts of the scattered field in each case. The identification has mainly been done through a comparison with Fig. 5.11 with the same crack orientations but in an isotropic material and Fig. 5.9 with no cracks but the same anisotropic material. In general the scattered fields are heavily deformed relative to the isotropic case. This is especially seen for the diffracted signals which in the isotropic case are of circular shape. In this figure the diffracted qL (DqL) signal due to the particular form of anisotropy takes the form of a rounded box. The diffracted qSV (DqSV) wave is less obvious. In the plots, the reflected qL (RqL) and qSV (RqSV) waves are seen as well as the quasi head (qH) wave and quasi Rayleigh (qR) wave. Especially in the upper plot, it is seen that in such materials, the diffracted echo may be weak or even missing due to the beam skewing.

Fig. 5.13 shows two examples of the scattered field from a circular cavity of radius $30\Delta x = 3\,\mathrm{mm}$. In the upper plot the incident field is that from a 0° probe with pulse signal $f(t;2)$ and $f_0 = 2\,\mathrm{MHz}$. The incident field in the lower plot is that from a 45° SV transducer with pulse signal as above. In both cases the characteristic scattered waves of longitudinal nature (outer) and transverse (inner) nature are seen. As the incident field passes the cavity, scattered waves creep around the surface of the cavity while shedding waves into the surrounding material. These disturbances are clearly seen in the plots. In the lower plot, note the small amplitude of the scattered longitudinal wave back towards

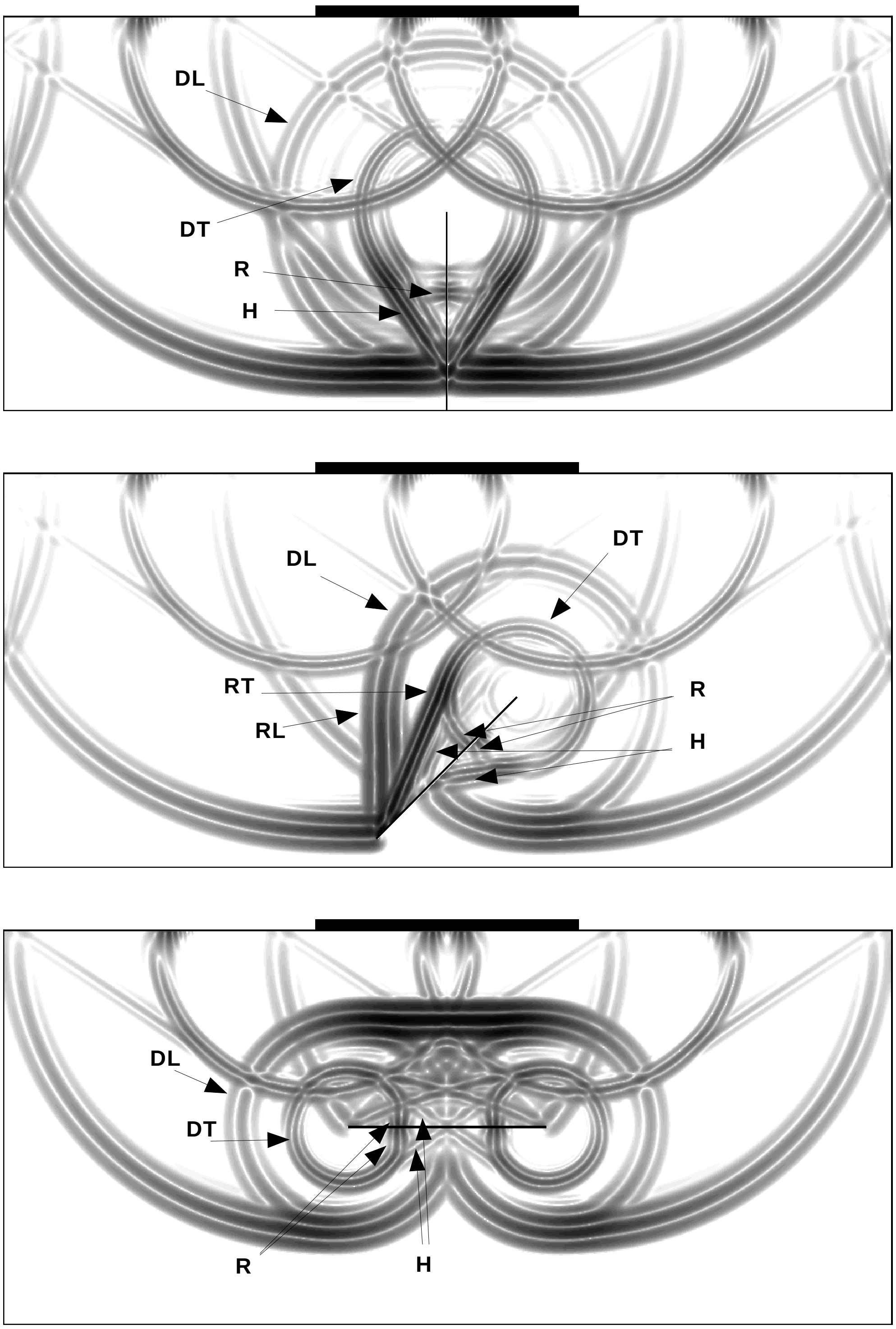


Figure 5.11: Scattered sound fields for different orientations of a rectangular crack in the case of a 0° incoming longitudinal wave in isotropic austenite. Pulse signal is $f(t;2)$ with $f_0 = 2\,\text{MHz}$ and the transducer width is 26.6 mm. The different types of scattered waves are identified. Crack height 20 mm and width 0.1 mm, except in the middle plot with width 0.2 mm. Times are $t = 6.8\,\mu\text{s}$ (upper and middle plot) and $t = 5.8\,\mu\text{s}$ (lower plot). See text for an explanation of abbreviations. Rectangular dimensions are 90 mm × 40 mm. Logarithmic scale is used with range -50 dB (white) to 0 dB (black) with 25 levels. $(\Delta x, \Delta t) = (10^{-4}\,\text{m}, 10^{-8}\,\text{s})$.

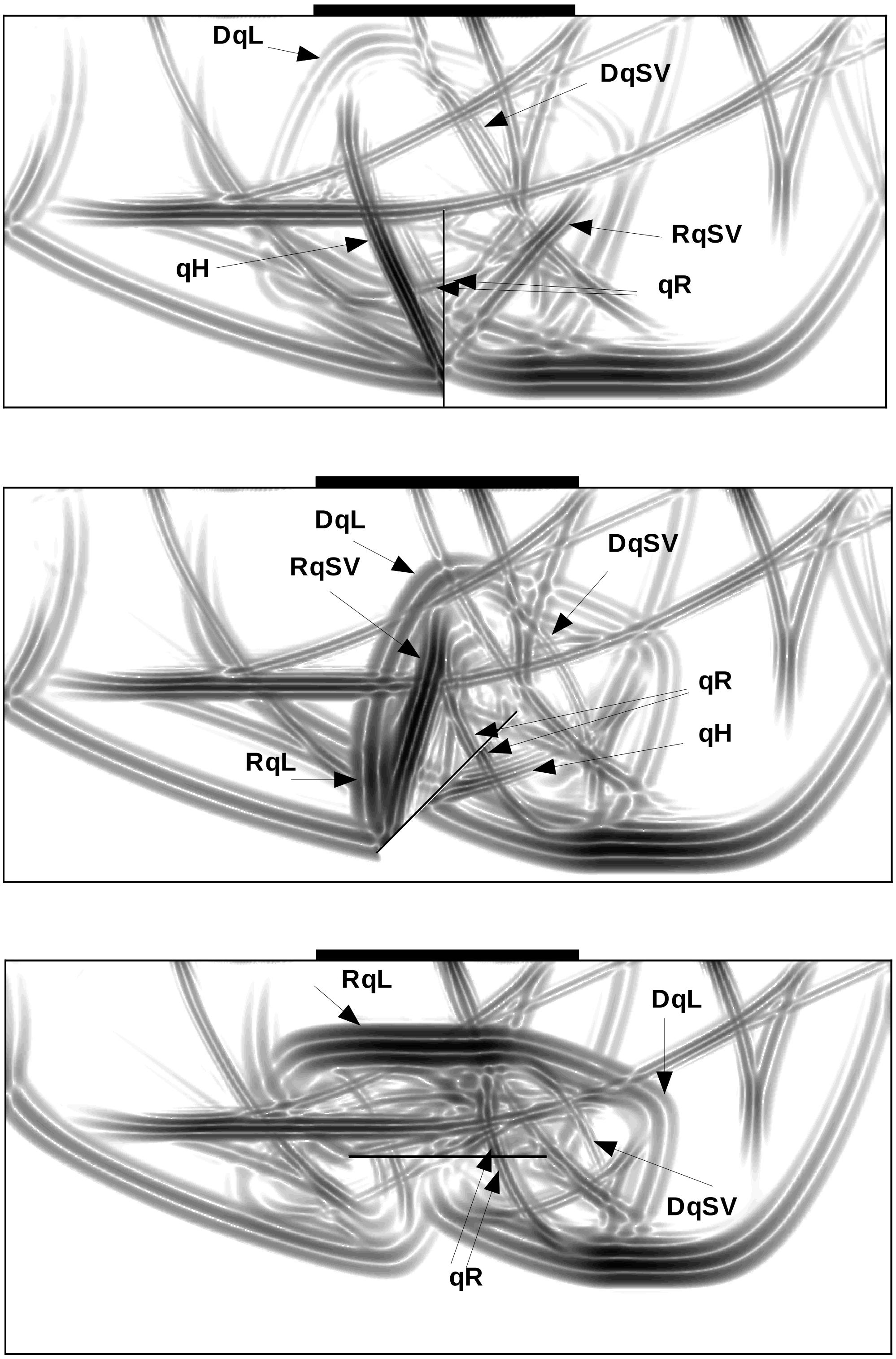


Figure 5.12: Examples of the scattered field from various rectangular crack orientations and transducer specifications as in Fig. 5.11 in transversely isotropic X 6 CrNi 18 12 rotated the Euler angle $\theta = -20°$. See text for an explanation of abbreviations. The different types of generated waves are identified. Crack height 20 mm and width = 0.1 mm, except middle plot with width 0.2 mm. Times are $t = 6.8\,\mu$s (upper and middle plot) and $t = 5.8\,\mu$s (lower plot). Logarithmic scale is used with range -50 dB (white) to 0 dB (black) with 25 levels. Material geometry is 90 mm $\times$ 40 mm. $(\Delta x,\, \Delta t) = (10^{-4}\,\text{m},\, 10^{-8}\,\text{s})$.

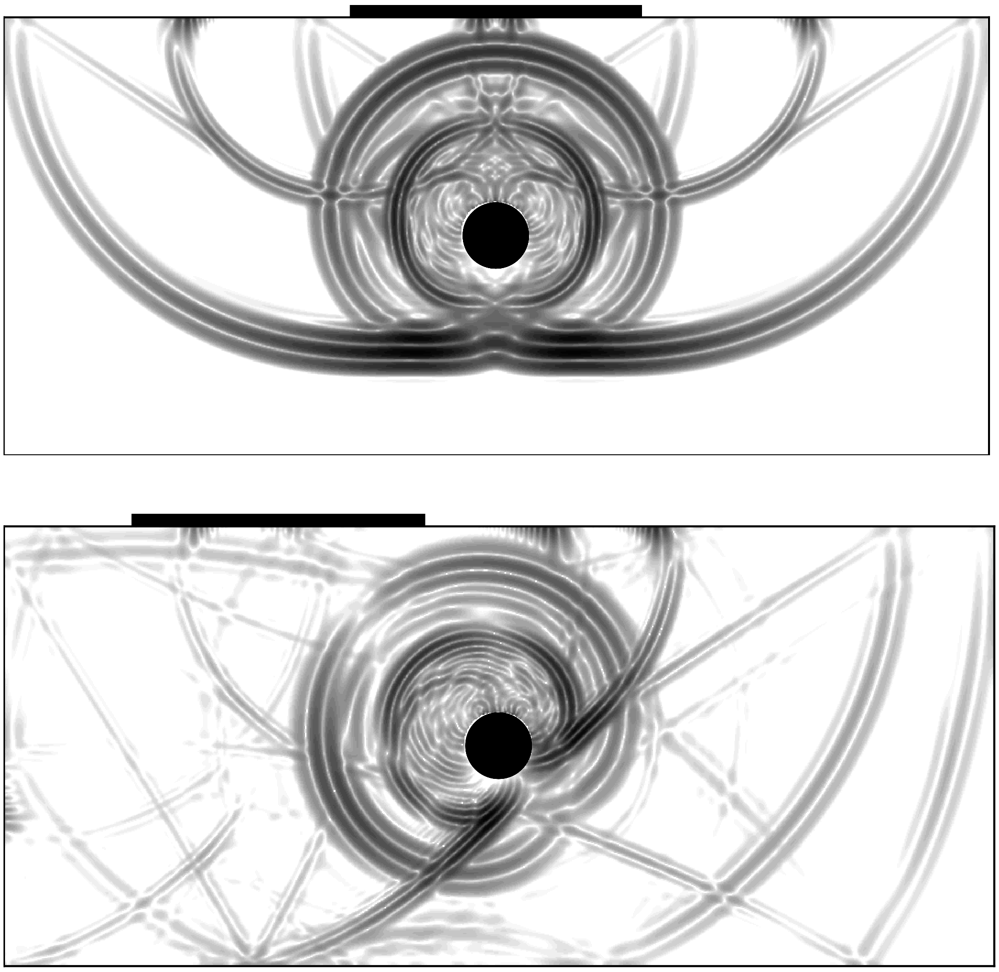

Figure 5.13: Examples of the scattered field from a circular cavity with radius $30\Delta x = 3\,\mathrm{mm}$ in isotropic austenite. Pulse signal is $f(t;2)$ with $f_0 = 2\,\mathrm{MHz}$ and transducer width is 26.6 mm. Both plots use a logarithmic scale from -50 dB (white) to 0 dB (black) with 25 levels. Material geometry in both cases is $90\,\mathrm{mm} \times 40\,\mathrm{mm}$. Upper plot: 0° probe and time is $t = 5.8\,\mu\mathrm{s}$. Lower plot: 45° SV probe and time is $t = 14\,\mu\mathrm{s}$. $(\Delta x,\, \Delta t) = (10^{-4}\,\mathrm{m},\, 10^{-8}\,\mathrm{s})$ in both plots.

the transducer from the cavity. This is characteristic for an incident transverse wave (compare with the case of normal incidence of a plane wave on a *plane* interface, where no mode conversion takes place either).

In this section, various examples have been given for the two defect types implemented in the modelling program. While the scattered fields in the isotropic case are identified with relative ease, it is demonstrated in the examples concerning anisotropic materials, that the identification of scattered fields may be quite a challenge.

## 5.3 A-scan modelling

This section is devoted to the modelling of A-scan signals and the presentation of these, i. e. the signal from echoes in the material recorded over time for a stationary receiver. This issue has already been briefly discussed in subsection 4.10. In a real ultrasonic NDT situation, the A-scan forms the basic information which the operator is provided with, and from these data the existence, position, size etc. of a defect must be determined. As indicated in contour plots in the last section, this is far from being a trivial task. While modelling tools developed for either amplitude modelling (such as PEDGE and PKIRCH mentioned in section 2.6) or wave propagation path (RAYTRAIM, also mentioned in section 2.6) are indeed valuable tools, a modelling tool which provides both facilities to the user may prove truly valuable for interpreting A-scans, optimizing inspection techniques etc., especially in anisotropic, inhomogeneous materials.

A simple model of an A-scan was formulated in subsection 4.10 when describing the transducer as a transmitter or receiver. The A-scan was calculated simply by averaging a velocity component over the (stress-free) surface of contact. If the receiver was an angled probe this was taken into account through a retarded time $t_{ret}$. Two drawbacks of this simple approach has been mentioned. The first was the stress-free surface of contact which could result in too high values (amplitudes), while the second was the shortcomings of the phase modelling for angled probes. Here, these drawbacks will be investigated to some extent through the comparison with results from another approach based on the *electromechanical reciprocity relations* to be presented below.

### 5.3.1 The electromechanical reciprocity relations

Especially within the area of analytic modelling [6, 13, 67, 76], the *electromechanical reciprocity relations* are used in different formulations to calculate a quantity which essentially represents the electric signal based on the knowledge of the corresponding mechanical state of the material. The previously described program SUNDT is an example of an approach using this method. The advantage of the method is that the transducer only needs to be modelled as a transmitter in order to obtain the A-scan. In this subsection, an attempt is made to adapt this method to the numerical approach used in this thesis. As noted above, the aim is to be able to compare the results of this (well-established) method to the simple A-scan model described in subsection 4.10. Furthermore, this development also allows a more direct comparison with the SUNDT program. These comparisons will be carried out in the next subsection

The presentation of the electromechanical reciprocity relations is based on [6, 8]. The theory is developed in the frequency domain or equivalently for time-harmonic fields of frequency $\omega$. The final result is then transformed to the time domain. We consider an elastic non-pieozelectric medium with two piezoelectric transducers on the surface as shown in Fig. 5.14. At this point the two illustrations in the figure should be considered identical except for the presence of a scatterer with a surface $S_F$ in the right illustration. The aim is to model the A-scan signal due to the presence of this scatterer for specified transmitter and receiver. The lower horizontal and the two vertical sides of the rectangles in the figure should be imagined moved to infinity, ie. the reflections from these boundaries are not taken into account.

In general, when acting as a transmitter, the transducer receives an electromagnetic field through the coaxial cable. When acting as a receiver the transducer gives raise to an electromagnetic field through the coaxial cable. The total fields are denoted by $\boldsymbol{E}$ (electric field) and $\boldsymbol{H}$ (magnetic field). The electromagnetic field is coupled to the elastodynamic fields $\boldsymbol{v}$ and $\boldsymbol{T}$ in the material through the piezoelectric coupling at the transducers.

The electric and magnetic fields satisfy Maxwell's equations written here in the frequency domain (or for time-harmonic fields)

$$-\nabla \times \tilde{\boldsymbol{E}} = \mathrm{i}\omega\boldsymbol{\mu} \cdot \tilde{\boldsymbol{H}} \tag{5.2a}$$

$$\nabla \times \tilde{\boldsymbol{H}} = \mathrm{i}\omega\boldsymbol{\epsilon} \cdot \tilde{\boldsymbol{E}} \tag{5.2b}$$

where a tilde ˜ denotes a Fourier transform in time. $\boldsymbol{\mu}$ is the symmetric second order permeability tensor and $\boldsymbol{\epsilon}$ is the symmetric second order permittivity tensor. These two tensors will, however, not be important in the following. In writing (5.2b) we have assumed that no electric sources are present inside the (integration) volume $S_0$ considered.

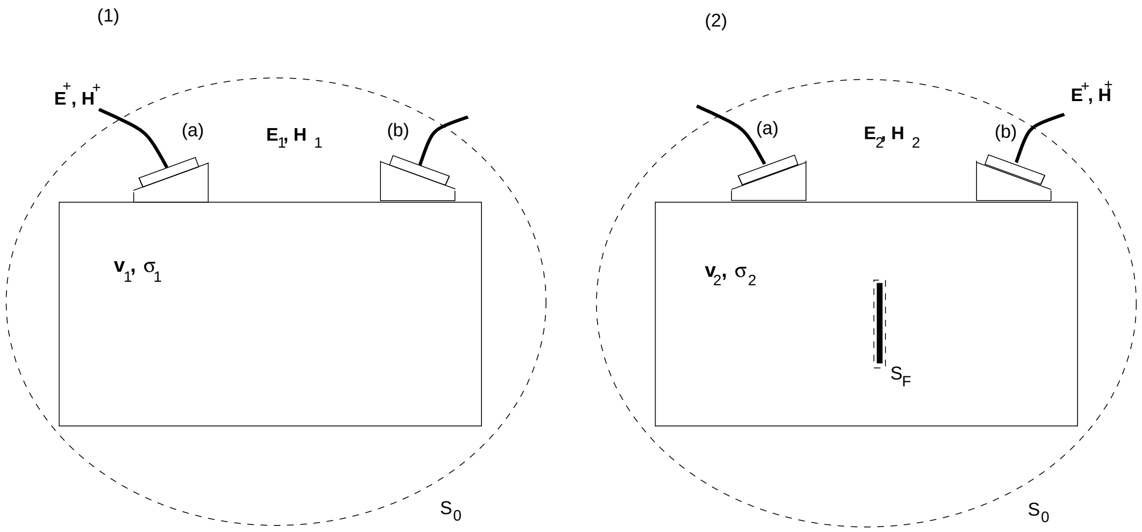


Figure 5.14: Illustration of the electromechanical reciprocity relations.

It may readily be shown that the elastodynamic equations (2.12) may be written in the following ordinary vector notation

$$\nabla \cdot \boldsymbol{\sigma} = \rho \frac{\partial \boldsymbol{v}}{\partial t} \tag{5.3a}$$

$$\nabla_s \boldsymbol{v} \equiv \frac{1}{2}(\nabla \boldsymbol{v} + (\nabla \boldsymbol{v})^T) = \boldsymbol{s} : \frac{\partial \boldsymbol{\sigma}}{\partial t} \tag{5.3b}$$

where the gradient operator $\nabla_s$ of a vector has been introduced for convenience. : means a double summation, i. e. $(\boldsymbol{s} : \partial\boldsymbol{\sigma}/\partial t)_{ij} = s_{ijkl}\partial\sigma_{kl}/\partial t$. Again we have assumed that there are no elastic sources in the volume $S_0 - S_F$. A Fourier transform of (5.3) results in

$$\nabla \cdot \tilde{\boldsymbol{\sigma}} = \mathrm{i}\omega\rho\tilde{\boldsymbol{v}} \tag{5.4a}$$

$$\nabla_s \tilde{\boldsymbol{v}} = \mathrm{i}\omega\boldsymbol{s} : \tilde{\boldsymbol{\sigma}} \tag{5.4b}$$

We now consider two different solutions to (5.2) and (5.4), state (1) with variables $\{\tilde{\boldsymbol{E}}_1, \tilde{\boldsymbol{H}}_1, \tilde{\boldsymbol{v}}_1, \tilde{\boldsymbol{\sigma}}_1\}$ and state (2) with variables $\{\tilde{\boldsymbol{E}}_2, \tilde{\boldsymbol{H}}_2, \tilde{\boldsymbol{v}}_2, \tilde{\boldsymbol{\sigma}}_2\}$. The two situations are shown in Fig. 5.14, left and right respectively. In state (1), transducer (a) acts as a transmitter in *the absence* of the scatterer and in state (2), transducer (b) acts as a transmitter in *the presence* of the scatterer. The electromagnetic fields from the two states may be inserted in (5.2) resulting in two sets of equations with subscripts (1) and (2). Multiply now the two equations in equation set (1) with $-\tilde{\boldsymbol{H}}_2$ and $\tilde{\boldsymbol{E}}_2$ respectively and add the two equations. Perform the same operation with the other equation set with subscripts reversed. Subtracting the two resulting equations results after some vector manipulation in Lorentz's reciprocity relation for electromagnetic fields

$$\nabla \cdot (\tilde{\boldsymbol{E}}_1 \times \tilde{\boldsymbol{H}}_2 - \tilde{\boldsymbol{E}}_2 \times \tilde{\boldsymbol{H}}_1) = 0 \tag{5.5}$$

We may perform the elastodynamic analog to (5.4) multiplying the two equations with $-\tilde{\boldsymbol{v}}_{(i)}$ and $\tilde{\boldsymbol{\sigma}}_{(i)}$ and obtain Lamb's reciprocity relation for elastodynamic fields

$$\nabla \cdot (\tilde{\boldsymbol{v}}_1 \cdot \tilde{\boldsymbol{\sigma}}_2 - \tilde{\boldsymbol{v}}_2 \cdot \tilde{\boldsymbol{\sigma}}_1) = 0 \tag{5.6}$$

Adding the two reciprocity relations result in

$$\nabla \cdot (\tilde{\boldsymbol{v}}_1 \cdot \tilde{\boldsymbol{\sigma}}_2 - \tilde{\boldsymbol{v}}_2 \cdot \tilde{\boldsymbol{\sigma}}_1 + \tilde{\boldsymbol{E}}_1 \times \tilde{\boldsymbol{H}}_2 - \tilde{\boldsymbol{E}}_2 \times \tilde{\boldsymbol{H}}_1) = 0 \tag{5.7}$$

in the volume enclosed between the surfaces $S_0$ and $S_F$. This is the fundamental equation[1] of the approach relating the electromagnetic fields to the elastodynamic fields. Integrating over this volume and using Gauss' theorem results in the following surface integral

$$\begin{aligned}
&\int_{coax(a)} (\tilde{\boldsymbol{E}}_1 \times \tilde{\boldsymbol{H}}_2 - \tilde{\boldsymbol{E}}_2 \times \tilde{\boldsymbol{H}}_1) \cdot \boldsymbol{n}\,\mathrm{d}S \quad + \\
&\int_{coax(b)} (\tilde{\boldsymbol{E}}_1 \times \tilde{\boldsymbol{H}}_2 - \tilde{\boldsymbol{E}}_2 \times \tilde{\boldsymbol{H}}_1) \cdot \boldsymbol{n}\,\mathrm{d}S \quad = \quad -\int_{S_F} (\tilde{\boldsymbol{v}}_1 \cdot \tilde{\boldsymbol{\sigma}}_2 - \tilde{\boldsymbol{v}}_2 \cdot \tilde{\boldsymbol{\sigma}}_1) \cdot \boldsymbol{n}\,\mathrm{d}S
\end{aligned} \tag{5.8}$$

where $\boldsymbol{n}$ is an outward surface normal to $S_0 + S_F$, that is, at $S_0$ it points outward, while at $S_F$ it points inward toward the scatterer. In summary, the elastodynamic variables are zero at the outer surface $S_0$, and the electromagnetic field only exist in the two coaxial cables as they are shielded.

In situation (1), in coaxial cable (a) the resulting electromagnetic fields are the sum of the incoming fields $\boldsymbol{E}^+$ and $\boldsymbol{H}^+$ and reflected fields due to any echoes from the medium. In coaxial cable (b) there only exist the transmitted fields. Thus for coaxial cable (a)

$$\tilde{\boldsymbol{E}}_1 = (1 + \Gamma_{aa})\tilde{\boldsymbol{E}}^+, \qquad \tilde{\boldsymbol{H}}_1 = (1 - \Gamma_{aa})\tilde{\boldsymbol{H}}^+$$

[1]The result (5.7) is also valid in the case of the material being piezoelectric. This is assumed in [8]. In this case (5.2) and (5.4) couple through the electric field $\tilde{\boldsymbol{E}}$ and the stress tensor $\tilde{\boldsymbol{\sigma}}$ making the derivation more comprehensive.

and for coaxial cable (b)

$$\tilde{\boldsymbol{E}}_1 = \Gamma_{ba}\tilde{\boldsymbol{E}}^+, \qquad \tilde{\boldsymbol{H}}_1 = -\Gamma_{ba}\tilde{\boldsymbol{H}}^+$$

Here $\Gamma_{aa}$ and $\Gamma_{ab}$ are the reflection and transmission coefficient due to the presence of the scatterer for (a) as a transmitter and (b) as a receiver. In situation (2) the situation is reversed. For coaxial cable (a)

$$\tilde{\boldsymbol{E}}_2 = \Gamma'_{ab}\tilde{\boldsymbol{E}}^+, \qquad \tilde{\boldsymbol{H}}_2 = -\Gamma'_{ab}\tilde{\boldsymbol{H}}^+$$

and for coaxial cable (b)

$$\tilde{\boldsymbol{E}}_2 = (1 + \Gamma'_{bb})\tilde{\boldsymbol{E}}^+, \qquad \tilde{\boldsymbol{H}}_2 = (1 - \Gamma'_{bb})\tilde{\boldsymbol{H}}^+$$

Inserting these expressions into (5.8) using the reciprocal relation $\Gamma_{ab} = \Gamma_{ba}$, we get

$$\delta\tilde{\Gamma}_{ba} = \Gamma'_{ba} - \Gamma_{ba} = \frac{1}{4G}\int_{S_F} (\tilde{\boldsymbol{v}}_1 \cdot \tilde{\boldsymbol{\sigma}}_2 - \tilde{\boldsymbol{v}}_2 \cdot \tilde{\boldsymbol{\sigma}}_1) \cdot \boldsymbol{n}\,\mathrm{d}S \tag{5.9}$$

where

$$G = -\frac{1}{2}\int_{coaxial-line} \tilde{\boldsymbol{E}}^+ \times \tilde{\boldsymbol{H}}^+ \cdot \boldsymbol{n}\,\mathrm{d}S \tag{5.10}$$

$G$ is not quite the electric power delivered to the transducer through the coaxial cable for time-harmonic fields due to a missing complex conjugate in $\tilde{\boldsymbol{H}}^+$. However for the TEM-mode (Transverse Electromagnetic Mode) present in the coaxial cable, the difference between the true power and $G$ is just a constant factor [49]. As only ratios are considered, this discrepancy may be neglected. For analytic approaches developed in the frequency domain the result (5.9) may naturally be incorporated into the approach thus providing essentially the electric signal directly, with SUNDT being an obvious example.

To be able to adapt this expression to our numerical approach (formulated in the time domain), we shall make an apparently rather drastic assumption. The factor $G$ in the expression (5.9) is simply neglected and instead the following expression is considered

$$\delta\tilde{\hat{\Gamma}}_{ba} = \int_{S_F} (\tilde{\boldsymbol{v}}_1 \cdot \tilde{\boldsymbol{\sigma}}_2 - \tilde{\boldsymbol{v}}_2 \cdot \tilde{\boldsymbol{\sigma}}_1) \cdot \boldsymbol{n}\,\mathrm{d}S \tag{5.11}$$

This expression can readily be transformed to the time domain, there directly making use of the elastodynamic variables $\boldsymbol{v}$ and $\boldsymbol{T}$ directly calculated by the numerical approach. The transformation is carried out by noting that the inverse Fourier transformation of a product of Fourier transformed functions is equal to the convolution of the two original functions, thus resulting in the following double integral

$$\delta\hat{\Gamma}_{ba}(t) = \int_{-\infty}^{\infty}\int_{S_F} (\boldsymbol{v}_1(t') \cdot \boldsymbol{\sigma}_2(t-t') - \boldsymbol{v}_2(t') \cdot \boldsymbol{\sigma}_1(t-t')) \cdot \boldsymbol{n}\,\mathrm{d}S\,\mathrm{d}t' \tag{5.12}$$

where as mentioned, $\boldsymbol{n}$ is the inward-directed normal vector. The impact of the above approximation is compared in the next subsection with SUNDT, which also uses this approach. In the analytic approach underlying the expression (5.9) is used, thus the factor $G$ is taken into account as well. It is however hoped, that by considering relative amplitudes, the neglect of the factor is minimized in the numerical approach. In the numerical approach, the two integrals in (5.12) are evaluated using the trapezoidal rule [64].

### 5.3.2 A-scan examples

In this subsection, A-scans are calculated and compared for the two methods (4.34) and (5.12). The examples are furthermore compared with results obtained by the SUNDT program. By including SUNDT in the comparison, a restriction to isotropic media is made. This is not a serious restriction, since the methods developed are not directly concerned with material properties. In all the examples, the pulse signal $f(t;2)$ with $f_0 = 2\,\text{MHz}$ has been used for the numerical program, while for the SUNDT program the frequency spectrum (2.36) is used with $f_0 = \Delta f = 2\,\text{MHz}$, see Fig. 2.3. These two signals were judged sufficiently similar in shape for a comparison. The results for the different examples considered in this subsection are summarized in Table 5.1 on page 90.

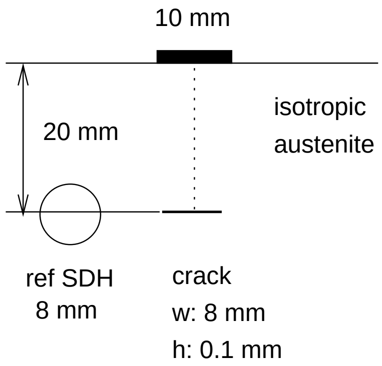


Figure 5.15: Illustration of the horizontal crack simulation.

Fig. 5.15 illustrates the simple example of normal incidence on a horizontal crack in isotropic austenite, Table 2.1. The scattered field may be seen in Fig. 5.11 (lower plot) for an equivalent problem. As reference echo, a sidedrilled hole (SDH) with a diameter of 8 mm and placed in the same depth is used. The resulting A-scans are shown in Fig. 5.16. The depth of the crack is 20 mm which is well outside the transducer near field length which is diameter$^2/4\lambda = (10\,\text{m})^2/(4 \times 2.9\,\text{mm}) = 8.7\,\text{mm}$ as also calculated by the SUNDT program.

The upper and middle plot are based on EFIT with the upper plot calculated using (4.33) and the middle plot using (5.12). The lower plot is the result generated by SUNDT. It has not been possible to extract the result from SUNDT in ASCII format for inclusion in the two upper plots. It was however possible to save the A-scan in a bitmap format, and this has simply been reproduced in the figure. This also applies to the following figures. The first strong signal is from the reflected longitudinal wave (L) at time $t = 2 \times 0.02\,m/5758\frac{m}{s} = 7\,\mu\text{s}$. The time of arrivals in the middle plot is delayed about $0.5\,\mu\text{s}$. This is due to the positioning of the surface $S_F$ for the integral in (5.12) around the defect. Ideally, this should be positioned right at the defect boundary. However, for the numerical evaluation the surface of integration has been made slightly larger. This observation also applies for the following figures. The weak signal at approximately time $t = 10.5\,\mu\text{s}$ are from the diffracted transverse waves (DT) at the two crack ends. As seen, the maximum amplitudes are practically identical with a value of 1.82 corresponding to 5.2 dB. For this example, the two approaches of calculating the A-scan give rather similar results.

The amplitude in the lower plot in Fig. 5.16 is normalized and therefore cannot be

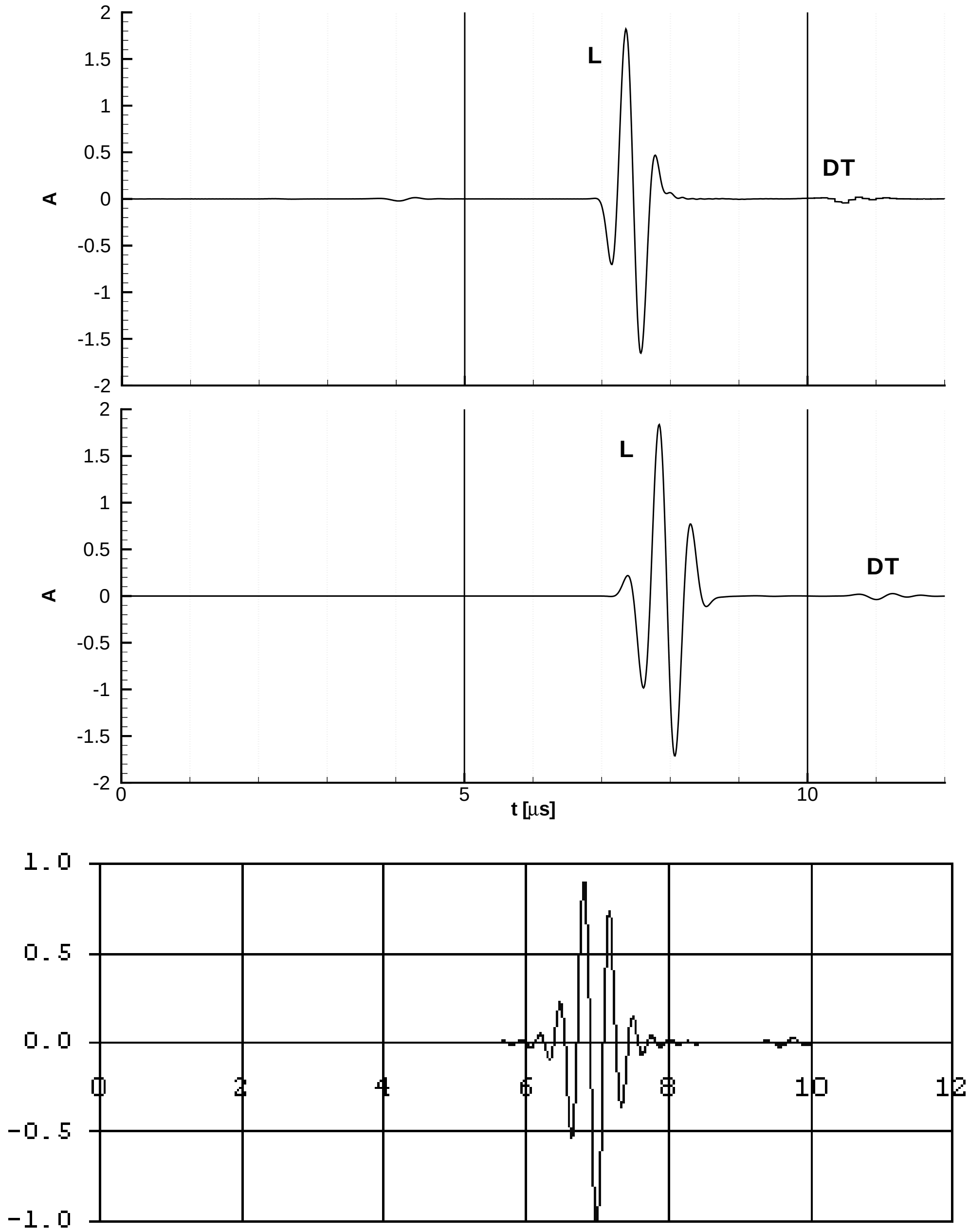


Figure 5.16: A-scans for a 0° probe with a horizontal crack in isotropic austenite, see Fig. 5.15. Upper and middle plot are based on the numerical approach EFIT, with the upper plot calculated using (4.33) and the middle plot using (5.12). The vertical scale on the two plots are relative to a 8 mm SDH, see text. Lower plot, also with $\mu$s as unit on time axis, is the result obtained from the SUNDT program. Vertical scale on lower plot is normalized.

compared with the two upper plots. As the pulse signal is centered around zero, see Fig. 2.3, the plot should be translated with approximately $1\,\mu$s to the right for ease of comparison. Concerning the plot, more oscillations are seen at the end for the longitudinal echo. The signal does however resemble the above signals, and especially the phases seem to be identical. Also the weak signal from the transverse wave is seen. The relative amplitude is 11.9 dB, which is about twice the above relative amplitudes. In the SUNDT program the defect has been scanned from a number of transducer positions on the surface in steps of 1 mm across the defect. The plot is shown for the A-scan with the largest amplitude, which has been obtained at a transducer position directly above the midpoint of the crack, shown with a dotted line in Fig. 5.15. In Fig. B.2 the results are shown for the transducer being displaced 1 mm relative to this maximum point (Fig. B.1 shows the window for the maximum transducer position, form which the lower plot in Fig. 5.16 has been extracted). As seen the echoes from the longitudinal and the diffracted transverse waves are in better agreement with the two upper plots in Fig. 5.15 in this case. From the figure, the maximum amplitude for this position is calculated as $11.9\,\mathrm{dB} - 20\log 0.65 \approx 8.2\,\mathrm{dB}$. Although the maximum amplitude is still rather large compared to the numerical approach above, it shows that the echo signal and amplitude is rather sensitive to the exact transducer position in this case. A few attempts of using the signal from a flat bottomed hole (FBH) at the same depth and with the same diameter in SUNDT failed due to an application error during a run.

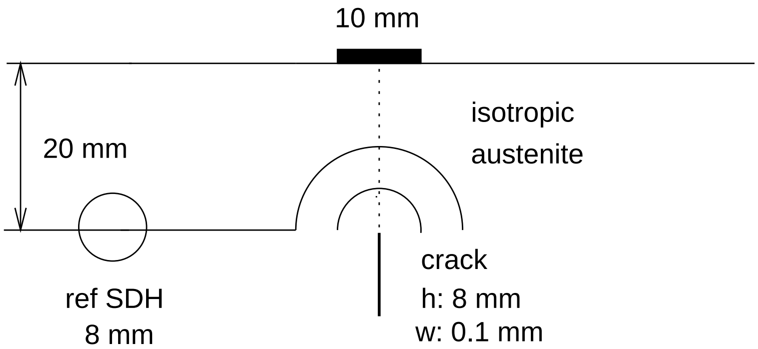


Figure 5.17: Illustration of a vertical crack and an unangled transducer.

The next example is concerned with a similar situation but with a vertical crack instead as shown in Fig. 5.17. Thus, here the echoes from the much weaker diffracted waves are considered. An example of the scattered field is seen in Fig. 5.11 (upper plot) for a similar problem. The corresponding A-scans are shown in Fig. 5.18. The organization of the A-scans are as before and will not be repeated here. In the upper plot, the two signals at times $t = 2\,\mu$s and $t = 4\,\mu$s are due to surface waves from the outgoing probe field itself travelling from one transducer end to the other and are therefore not important. At time $t = 7\,\mu$s the signal from the upper tip diffracted longitudinal wave (UDL) is observed. At time $t = 10\,\mu$s the signal from the lower tip diffracted longitudinal wave (LDL) is observed immediately followed by the upper tip diffracted transverse wave. The shown distorted signal is the superposition of the two waves. Again, there is a nice resemblance between the upper and middle plot. Remembering that the signal in the lower should be translated approximately $1\,\mu$s, the same signals are identified. However, here the second signal has a higher amplitude. The third signal has not been identified. The phases in the different plots are again similar. The upper and middle plot have the relative amplitudes -25.2 dB and -26.0 dB respectively. SUNDT reported a relative amplitude of -38.9 dB. The larger values resulting from the numerical approach might be explained by the fact that the modelled crack in the numerical approach has a finite width (0.1 mm) while SUNDT models an infinitely thin crack. The small horizontal surface might in this case result in a larger echo.

The last two examples are concerned with angled probes. Fig. 5.19 shows the situation of a vertical crack with a 45° L transducer with the corresponding A-scans shown in Fig. 5.20. The first signals (up to time $t = 6\,\mu$s) in the upper plot are as before not relevant for this comparison. The first signal of interest is at time $t = 11\,\mu$s where the upper tip diffracted longitudinal wave (UDL) arrives. The lower tip diffracted longitudinal wave (UDL) arrives at time $t = 14\,\mu$s. The upper tip diffracted transverse wave (UDT) arrives at time $t = 15.5\,\mu$s. In the upper plot this is somewhat distorted by the reflected longitudinal wave from the backwall, indicated by an (N) for noise. Apart from this noise there seems to be a good correspondence between the two plots. Thus, the simple A-scan model (4.33) appears to handle the phase question raised earlier sufficiently well for this example. The two waves are also found in the lower plot, although SUNDT does report earlier time of arrivals (even after taking the time translation into account). As in the previous case, the lower tip diffracted longitudinal wave (LDL) has a larger amplitude than the diffracted longitudinal wave. The phases are again similar in the three plots. Relative amplitudes for the upper and middle plots are -20.1 dB and -21.1 dB respectively, while the SUNDT program reports a maximum value of $-15.9\,\text{dB} + 20\log|-0.21| = -29.5\,\text{dB}$. This calculation is performed since SUNDT (by user request) has scanned the surface at different positions and the different A-scan plots are then reported relative to the A-scan with the largest amplitudes. The A-scan of interest to our problem has a maximum numerical value of 0.21 relative to the maximum value over all A-scans (-15.9 dB). Concerning this value, it should be noted, that SUNDT optimizes the reference transducer angle for maximum reference echo (in this case 42.9°). This may have an influence on the smaller SUNDT result relative to the EFIT results which are based on a fixed transducer angle of 45° for the reference signal.

The last example considered is similar to the previous example, except that a different transmitter and receiver are now used. They are placed on each side of the vertical crack with the same distance as shown in Fig. 5.21 and they are both 45° L probes. Of course, a large similarity with the last example is expected. This example was considered mainly due to the use of two transducers as opposed to the previous examples. A smaller time interval is considered in order to avoid signals from reflections at the vertical boundaries in the upper plot. The corresponding A-scans are shown in Fig. 5.22. Although a few attempts were performed for this example it was not possible to obtain a result from the SUNDT program. This may probably be due to lack of experience of the author in using the program. The first signal arriving at time $t = 8\,\mu$s in the upper plot is a head wave (H) travelling along the surface from the transmitter to the receiver. This is followed by the upper tip diffracted longitudinal wave (UDL) arriving at time $t = 11.5\,\mu$s. At time $t = 13.5\,\mu$s, the lower tip diffracted longitudinal wave arrives at the receiver (LDL). Shortly after, the Rayleigh waves propagating along the surface are detected by the receiver, making the signal a combination of the two wave types. In the middle plot, the surface localized head wave and Rayleigh wave are not seen, since they don't contribute to

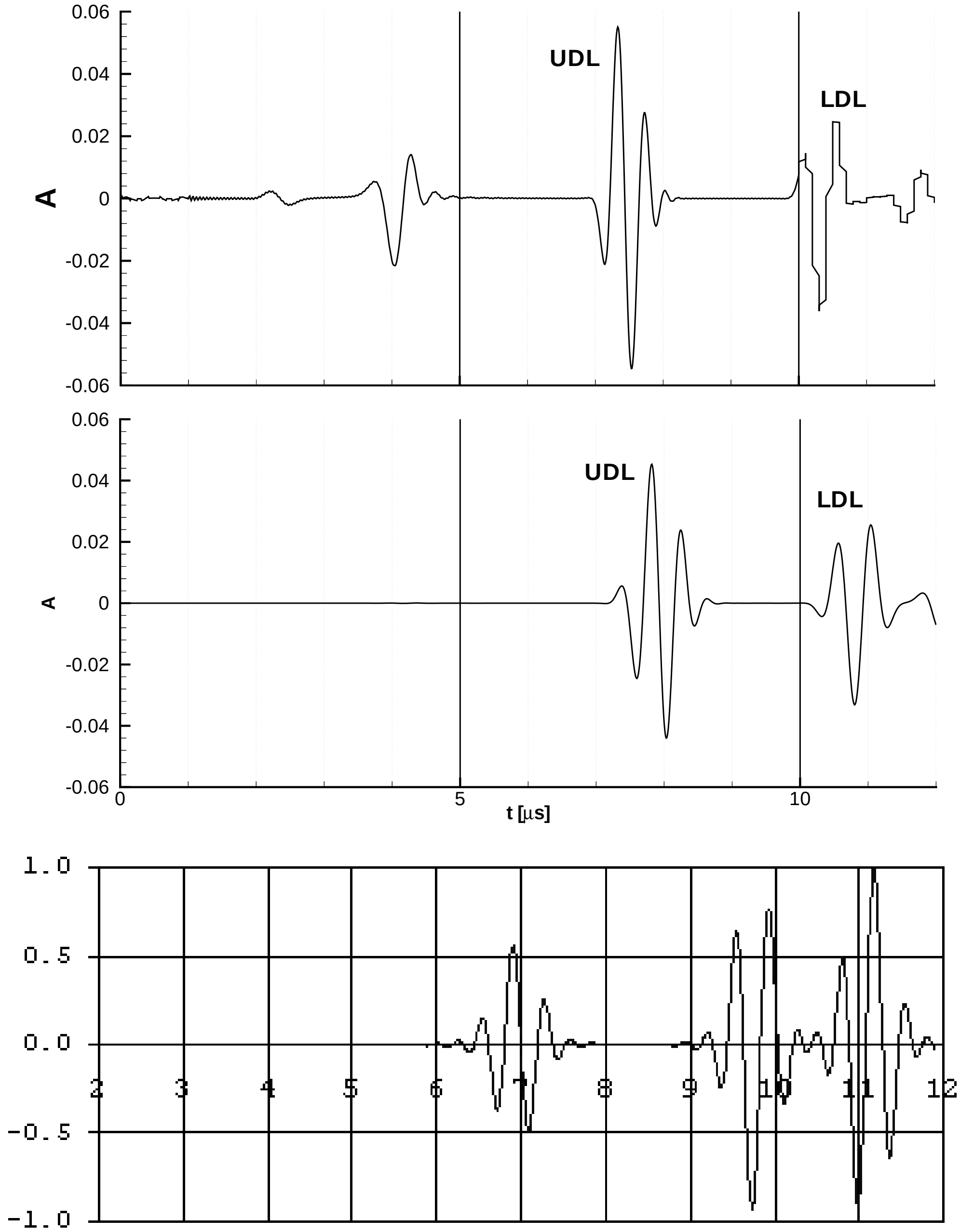


Figure 5.18: A-scans for a 0° probe with a vertical crack in isotropic austenite, see Fig. 5.17. Upper and middle plot are based on EFIT, with the upper plot calculated using (4.33) and middle plot using (5.12). The vertical scale on the two plots are relative to a 8 mm SDH. Lower plot, also with $\mu$s as unit on time axis, is the result obtained from the SUNDT program. Vertical scale on lower plot is normalized.

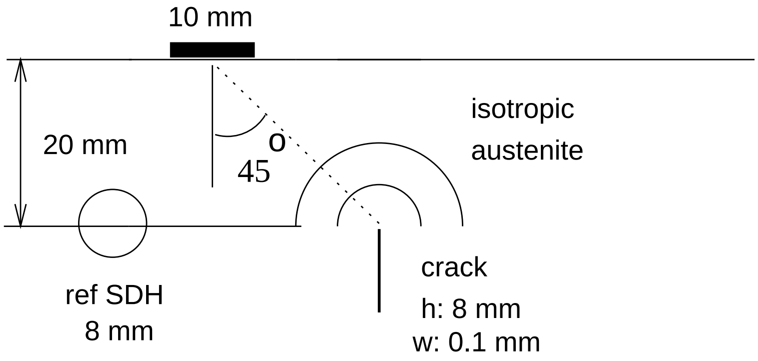


Figure 5.19: Illustration of a vertical crack and a 45° L transducer.

the surface integral of the crack. However, the two relevant signals from the two diffracted waves are clearly seen. The absence of the Rayleigh wave in the lower plot might explain the discrepancy between the signals from the last diffracted longitudinal wave. The lower plot is similar to the middle plot in Fig. 5.20 as expected. Again, the phases of the waves in the two plots appear to be in agreement. The amplitudes in the upper and middle plots are -27.6 dB and -30.5 dB respectively.

Although the number of examples presented here is not large, it seems appropriate at this point to draw some conclusions concerning the different methods of calculating A-scans. In general, the EFIT related methods (4.34) and (5.12) must be said to yield approximately the same results. This is true for both the shape of the calculated A-scans as well as the relative amplitudes. Since the two methods are fundamentally different, it may be stated that they in this way validate each other, at least within the EFIT framework. Thus, when using relative amplitudes, (4.34) appears to give reasonable results. Also the matter of correct phase modelling for angled probes seems to be handled reasonably well by (4.34). The two methods have been compared to results from the SUNDT program. There are discrepancies between the reported relative amplitudes and possible explanations have been given. However, the shapes and content of the A-scans have a large degree of similarity.

| Situation | Figures | EFIT (4.34) | EFIT (5.12) | SUNDT |
|---|---|---|---|---|
| Horiz. crack, 0° (T) | 5.15 and 5.16 | 5.2 dB | 5.2 dB | 11.9 dB |
| Ver. crack, 0° (T) | 5.17 and 5.18 | -25.2 dB | -26.9 dB | -38.9 dB |
| Ver. crack, 45° L (T) | 5.19 and 5.20 | -20.1 dB | -21.1 dB | -29.5 dB |
| Ver. crack, 45° L (T) and (R) | 5.21 and 5.22 | -27.6 dB | -30.5 dB | |

Table 5.1: Maximum amplitudes reported by the two EFIT approaches and the SUNDT program for different defect and probe types.

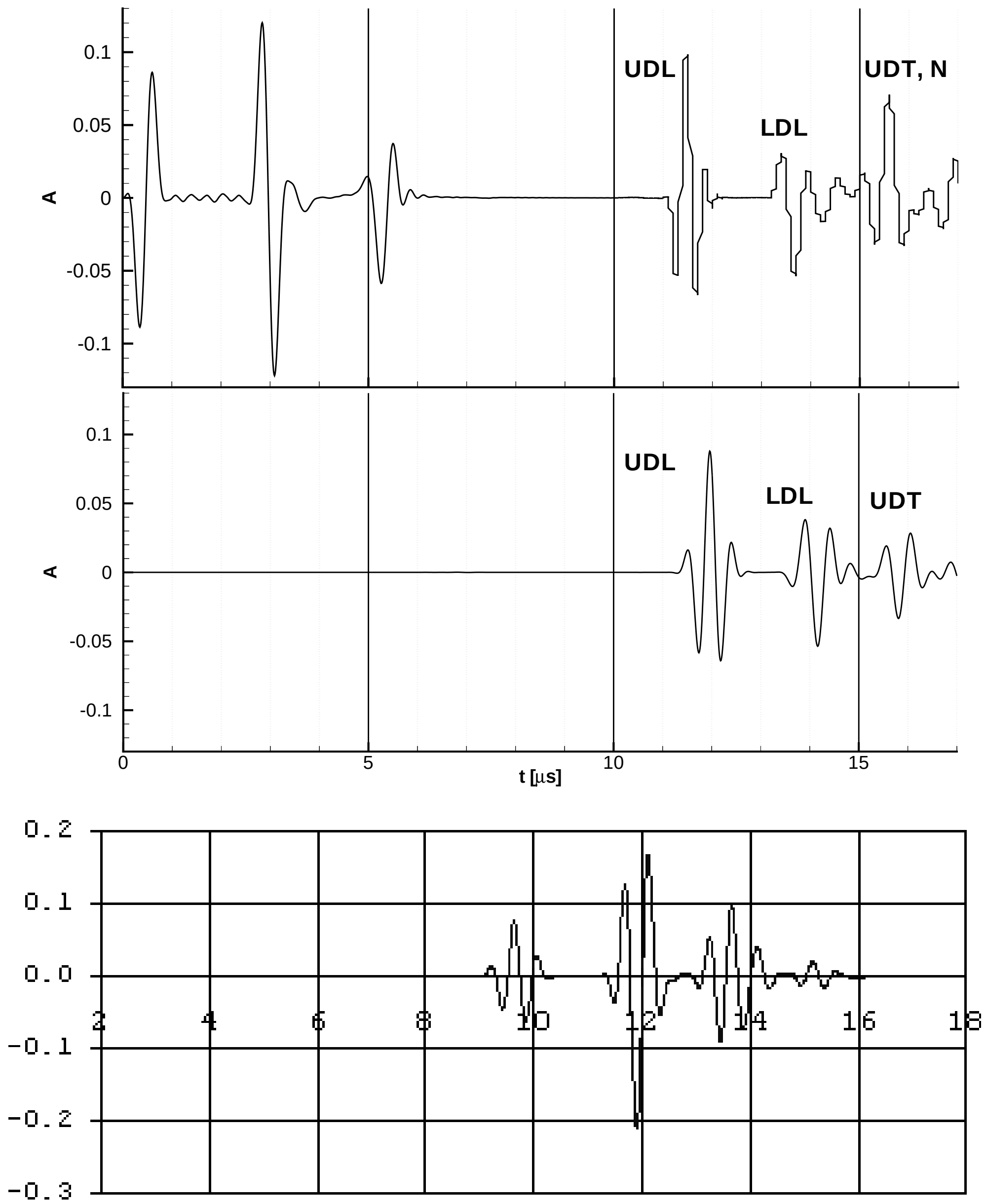


Figure 5.20: A-scans for a 45° L transducer with a vertical crack in isotropic austenite, see Fig. 5.19. Upper and middle plot are based on EFIT, with the upper plot calculated using (4.33) and middle plot using (5.12). The vertical scale on the two plots are relative to a 8 mm SDH. Lower plot, also with $\mu$s as unit on time axis, is the result obtained from the SUNDT program. Vertical scale on lower plot is not comparable to the upper plots.

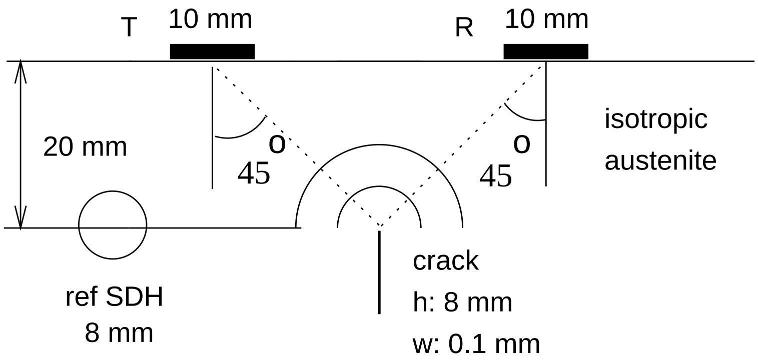


Figure 5.21: Illustration of a vertical crack with separate 45° L transmitter and receiver.

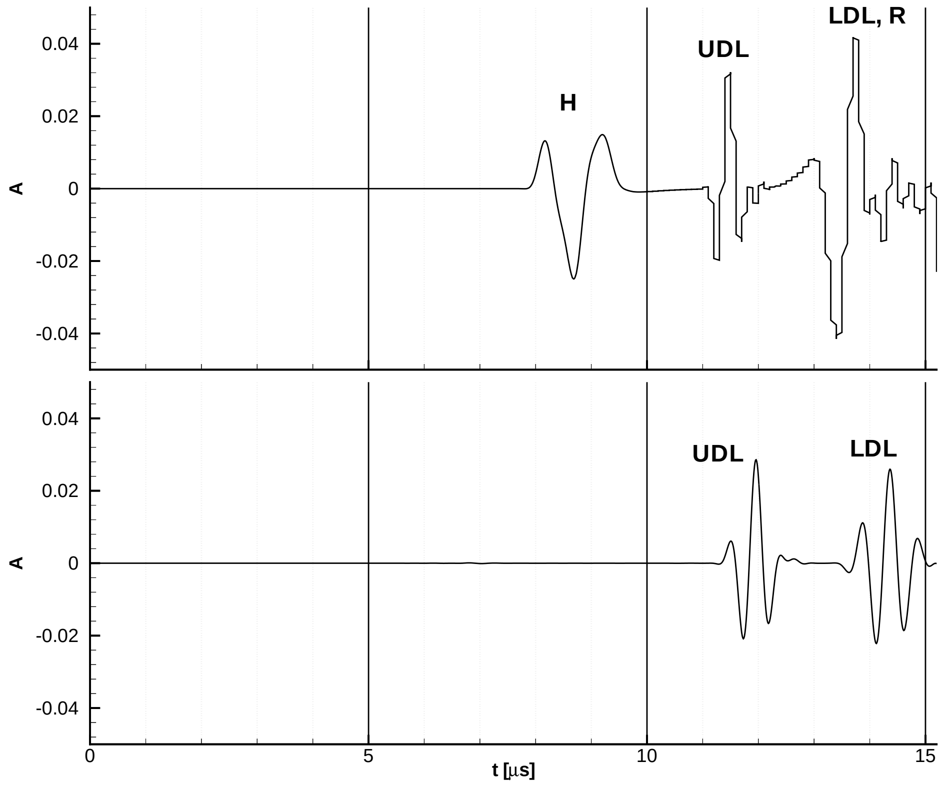


Figure 5.22: A-scans for a vertical crack with separate 45° L transmitter and receiver. Both plots are based on EFIT, with the upper plot calculated using (4.33) and lower plot using (5.12). The vertical scale on the two plots are relative to a 8 mm SDH.